Optics EXPRESS

Volumetric rendering and metrology of spherical gradient refractive index lens imaged by angular scan optical coherence tomography system

JIANING YAO,[1,*] KEVIN P. THOMPSON,[1,2,3] BIN MA,[1] MICHAEL PONTING,[4] AND JANNICK P. ROLLAND[1]

[1]*The Institute of Optics, University of Rochester, Rochester, NY 14627, USA*
[2]*Synopsys Inc., 3 Graywood Lane, Pittsford, NY 14534, USA*
[3]*Deceased*
[4]*PolymerPlus LLC, Valley View, OH 44125, USA*
[*]*jyao@optics.rochester.edu*

Abstract: In this paper, we develop the methodology, including the refraction correction, geometrical thickness correction, coordinate transformation, and layer segmentation algorithms, for 3D rendering and metrology of a layered spherical gradient refractive index (S-GRIN) lens based on the imaging data collected by an angular scan optical coherence tomography (OCT) system. The 3D mapping and rendering enables direct 3D visualization and internal defect inspection of the lens. The metrology provides assessment of the surface geometry, the lens thickness, the radii of curvature of the internal layer interfaces, and the misalignment of the internal S-GRIN distribution with respect to the lens surface. The OCT metrology results identify the manufacturing defects, and enable targeted process development for optimizing the manufacturing parameters. The newly fabricated S-GRIN lenses show up to a 7x spherical aberration reduction that allows a significantly increased utilizable effective aperture.

OCIS codes: (120.0120) Instrumentation, measurement, and metrology; (110.4500) Optical coherence tomography; (120.4630) Optical inspection; (110.0110) Imaging systems.

References and links

1. R. N. Zahreddine, R. S. Lepkowicz, R. M. Bunch, E. Baer, and A. Hiltner, "Beam shaping system based on polymer spherical gradient refractive index lenses," Proc. SPIE **7062**, 706214 (2008).
2. P. Kotsidas, V. Modi, and J. M. Gordon, "Nominally stationary high-concentration solar optics by gradient-index lenses," Opt. Express **19**(3), 2325–2334 (2011).
3. R. A. Flynn, E. F. Fleet, G. Beadie, and J. S. Shirk, "Achromatic GRIN singlet lens design," Opt. Express **21**(4), 4970–4978 (2013).
4. J. Yao, P. Meemon, M. Ponting, and J. P. Rolland, "Angular scan optical coherence tomography imaging and metrology of spherical gradient refractive index preforms," Opt. Express **23**(5), 6428–6443 (2015).
5. S. Ji, K. Yin, M. Mackey, A. Brister, M. Ponting, and E. Baer, "Polymeric nanolayered gradient refractive index lenses: technology review and introduction of spherical gradient refractive index ball lenses," Opt. Eng. **52**(11), 112105 (2013).
6. M. Ponting, A. Hiltner, and E. Baer, "Polymer nanostructures by forced assembly: process, structure and properties," Macromol. Symp. **294**(1), 19–32 (2010).
7. P. Lalanne and D. Lemercier-Lalanne, "On the effective medium theory of subwavelength periodic structures," J. Mod. Opt. **43**(10), 2063–2085 (1996).
8. P. Meemon, J. Yao, K. S. Lee, K. P. Thompson, M. Ponting, E. Baer, and J. P. Rolland, "Optical coherence tomography enabling non destructive metrology of layered polymeric GRIN material," Sci. Rep. **3**, 1709 (2013).
9. T. Yamagishi, K. Fujii, and I. Kitano, "Gradient-index rod lens with high N.A," Appl. Opt. **22**(3), 400–403 (1983).
10. W. A. Reed, M. F. Yan, and M. J. Schnitzer, "Gradient-index fiber-optic microprobes for minimally invasive in vivo low-coherence interferometry," Opt. Lett. **27**(20), 1794–1796 (2002).
11. Y. Koike, Y. Takezawa, and Y. Ohtsuka, "New interfacial-gel copolymerization technique for steric GRIN polymer optical waveguides and lens arrays," Appl. Opt. **27**(3), 486–491 (1988).

#264357 http://dx.doi.org/10.1364/OE.24.019388
Journal © 2016 Received 15 Jun 2016; revised 1 Aug 2016; accepted 1 Aug 2016; published 11 Aug 2016

Optics EXPRESS

12. M. Choma, M. Sarunic, C. Yang, and J. Izatt, "Sensitivity advantage of swept source and Fourier domain optical coherence tomography," Opt. Express **11**(18), 2183–2189 (2003).
13. J. F. de Boer, B. Cense, B. H. Park, M. C. Pierce, G. J. Tearney, and B. E. Bouma, "Improved signal-to-noise ratio in spectral-domain compared with time-domain optical coherence tomography," Opt. Lett. **28**(21), 2067–2069 (2003).
14. P. Ossowski, A. Raiter-Smiljanic, A. Szkulmowska, D. Bukowska, M. Wiese, L. Derzsi, A. Eljaszewicz, P. Garstecki, and M. Wojtkowski, "Differentiation of morphotic elements in human blood using optical coherence tomography and a microfluidic setup," Opt. Express **23**(21), 27724–27738 (2015).
15. P. Tankam, Z. He, Y. J. Chu, J. Won, C. Canavesi, T. Lepine, H. B. Hindman, D. J. Topham, P. Gain, G. Thuret, and J. P. Rolland, "Assessing microstructures of the cornea with Gabor-domain optical coherence microscopy: pathway for corneal physiology and diseases," Opt. Lett. **40**(6), 1113–1116 (2015).
16. A. Curatolo, M. Villiger, D. Lorenser, P. Wijesinghe, A. Fritz, B. F. Kennedy, and D. D. Sampson, "Ultrahigh-resolution optical coherence elastography," Opt. Lett. **41**(1), 21–24 (2016).
17. Y. Verma, K. Rao, M. Suresh, H. Patel, and P. Gupta, "Measurement of gradient refractive index profile of crystalline lens of fish eye in vivo using optical coherence tomography," Appl. Phys. B **87**(4), 607–610 (2007).
18. S. Ortiz, P. Pérez-Merino, E. Gambra, A. de Castro, and S. Marcos, "In vivo human crystalline lens topography," Biomed. Opt. Express **3**(10), 2471–2488 (2012).
19. S. Ortiz, D. Siedlecki, I. Grulkowski, L. Remon, D. Pascual, M. Wojtkowski, and S. Marcos, "Optical distortion correction in optical coherence tomography for quantitative ocular anterior segment by three-dimensional imaging," Opt. Express **18**(3), 2782–2796 (2010).
20. J. Yao, P. Meemon, K. S. Lee, and J. P. Rolland, "Nondestructive metrology by optical coherence tomography empowering manufacturing iterations of layered polymeric optical materials," Opt. Eng. **52**(11), 112111 (2013).
21. J. Yao, J. Huang, P. Meemon, M. Ponting, and J. P. Rolland, "Simultaneous estimation of thickness and refractive index of layered gradient refractive index optics using a hybrid confocal-scan swept-source optical coherence tomography system," Opt. Express **23**(23), 30149–30164 (2015).
22. M. Born and E. Wolf, Principles of Optics (Cambridge University Press, 1998).
23. K. Karnowski, I. Grulkowski, N. Mohan, I. Cox, and M. Wojtkowski, "Quantitative optical inspection of contact lenses immersed in wet cell using swept source OCT," Opt. Lett. **39**(16), 4727–4730 (2014).

1. Introduction

The rapid expansion of modern optical components towards light weight, compact volume yet efficient aberration correction stimulates the investigation of gradient refractive index (GRIN) materials [1–3]. An intriguing type of GRIN structure to pursue is spherical GRIN (S-GRIN) lenses whose GRIN profile is symmetric about a point and therefore compositions of the same refractive index reside on spheres [4]. Many species have developed S-GRIN eye lenses in nature to possess greater focusing capability and high imaging quality with reduced counts of optical elements. For instance, a human crystalline lens consists of some 22,000 curved protein layers with gradually varying protein-water ratios across layers to form a gradient refractive index profile with an overall variation (Δn) of ~0.03. Inspired by the biological S-GRIN structure, a unique manufacturing process in fabricating S-GRIN lenses based on nanolayered films was developed at Case Western Reserve University and Naval Research Laboratory [5,6]. Typically 50 μm thick, each film contains 4097 nanolayers that are produced by multi-layer coextrusion of two polymers with substantially different refractive indices. The bulk film is transparent and has a refractive index that is approximately the volumetric average of the indices of the constituent polymers [7]. Therefore, by tuning the volumetric ratio of the co-polymers, a library of films with varying refractive indices can be produced. Through the compression-molding of a film stack arranged to meet a GRIN prescription, a flat axial GRIN sheet may be formed and subsequently thermoformed into a curved S-GRIN preform, which is finally diamond-turned into an S-GRIN lens [8]. This S-GRIN manufacturing approach enables a widely expanded range of achievable internal refractive index distribution compared to traditional interdiffusion [9], deposition [10], or sol-gel GRIN fabrication techniques [11].

Of paramount importance to the advancement of the S-GRIN manufacturing process refinements is an effective metrology tool capable of nondestructive inspection of the S-GRIN optics. Optical coherence tomography (OCT) fulfills such a role as a high-resolution three-dimensional (3D) imaging technique, particularly with the advancement of Fourier domain OCT (FD-OCT) [12,13], which utilizes broadband spectral interferometry to achieve superb depth sectioning with high sensitivity and high speed. FD-OCT has been extensively

Optics EXPRESS

developed for minuscule characterizations in biomedical imaging [14–16] to assist in precise diagnosis and treatment. The capability of FD-OCT for material metrology is drawing increasing attention in recent years. Several authors have reported using FD-OCT to reconstruct GRIN profiles of crystalline lenses [17,18]. To account for the optical distortion caused by ray deviations upon refraction at different media interfaces of the eye, Ortiz et al. investigated a 3D refraction correction algorithm applied in anterior segment OCT imaging [19]. In our prior work, we demonstrated the development of a swept-source OCT (SS-OCT) system for the inspection of flat axial GRIN optics [8,20,21] and an angular-scan OCT system for the metrology of curved S-GRIN preforms [4] that serve as the precursors to the final lenses. In this article, we report on the investigation of the 3D metrology and image rendering methodology developed for nondestructive, volumetric characterization and visualization of final S-GRIN lenses based on the angular-scan OCT system. We first provide the specifications of an S-GRIN lens imaged by angular-scan OCT in Section 2; the 3D mapping, rendering and metrology method is described in Section 3; in Section 4, we demonstrate the image rendering and metrology results of the S-GRIN lens, followed by a discussion in Section 5; finally, we conclude the paper in Section 6.

2. Specifications of plano-convex S-GRIN lens

Meniscus S-GRIN preforms whose surfaces and film layers inside were nominally concentric spheres were characterized by the angular-scan OCT system in [4]. In this paper, the same system was utilized to inspect a plano-convex S-GRIN lens that was cut out of a 3.2 mm thick S-GRIN preform composed of 128 layers [4].

As shown in Figs. 1(a) and 1(b), diamond turning was performed on the concave side of the preform (yellow dashed line) to reduce the center thickness by 0.1 ± 0.025 mm and form a plano surface. The convex surface of the preform was also diamond turned to meet the specified radius of curvature, which may differ from the preform, but also to suppress any residual surface deformation of the final preform. Nominally, by diamond turning 0.1 mm thick material uniformly from the convex surface of the preform, the radius of curvature of the convex surface decreases from 20.1 (± 0.15) mm in the preform to 20 (± 0.02) mm in the lens; therefore, the index contours within the S-GRIN lens remain concentric with the convex lens surface. In practice, however, the material removed from the convex surface of the preform may not be a uniformly thick shell, which results in a shift of the center of curvature of the convex lens surface from that of the S-GRIN distribution. In this case, the internal layers of the lens are no longer concentric with the convex surface; further determination relies on using the angular scan OCT to probe into the internal structure of the part. Additionally, after diamond turning the preform, the center thickness of the part reduces from 3.2 ± 0.015 mm to 3.0 ± 0.05 mm in the final lens, which contains 120 film layers. The composition of these film layers is linearly varied every 4 to 5 layers typically, based on a prescribed GRIN distribution recipe, from 74%/26% PMMA/SAN17 at the convex vertex to 14%/86% PMMA/SAN17 at the plano vertex. The corresponding group refractive index was estimated to increase from 1.5087 to 1.5554 (at the center wavelength of the OCT system, i.e., 1318 nm) across the total center thickness of the lens as shown in Fig. 1(d). The lens diameter is specified to be 19.3 mm with a minimum clear aperture of 18 mm. A photograph of the S-GRIN lens is shown in Fig. 1(c).

The nominal focal length of the lens at 633 nm is 35.6 mm and the F/# is 1.83 working at infinite conjugate. The nominal RMS wavefront error transmitted through the S-GRIN lens in this case is predicted to be 0.07 waves on axis, which shows well-corrected spherical aberration compared to a homogeneous singlet lens. The over-corrected spherical aberration induced by the internal S-GRIN distribution compensates for the under-corrected spherical aberration caused by the plano-convex surface geometry.

Optics EXPRESS

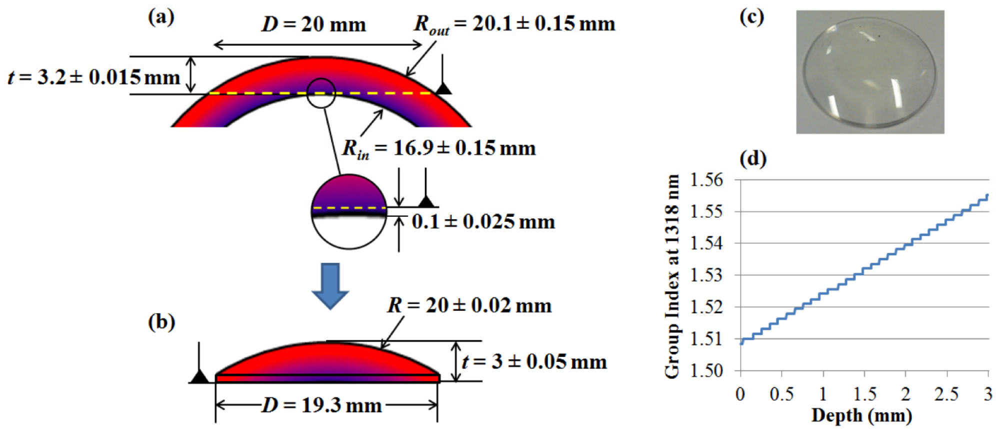

Fig. 1. Geometrical specifications of (a) an S-GRIN preform and (b) an S-GRIN lens cut out of the preform (the color scheme is to indicate the S-GRIN profile). (c) A photograph of an S-GRIN lens. (d) Estimated refractive index profile of the lens through its center thickness from material composition.

3. Method

The layout of the angular-scan OCT system was detailed in [4]. As shown in Fig. 2, the system builds on the instrumentation of an SS-OCT sample probe scanning in polar mode (θ) and a sample platform rotating azimuthally (ϕ), the combination of which enables the sample beam to maintain close to normal incidence on a spherical sample surface during 3D scans. Because of the near-normal incidence, high signal-to-noise ratio (SNR) is achieved across the imaging field. The angular-scan OCT imaging is directly acquired in spherical coordinates as shown in Fig. 3(b). Thus, we developed a method to map and render the 3D data set in Cartesian space for true-scale visualization and inspection of the volumetric geometry of S-GRIN lenses with the protocol summarized in Fig. 3.

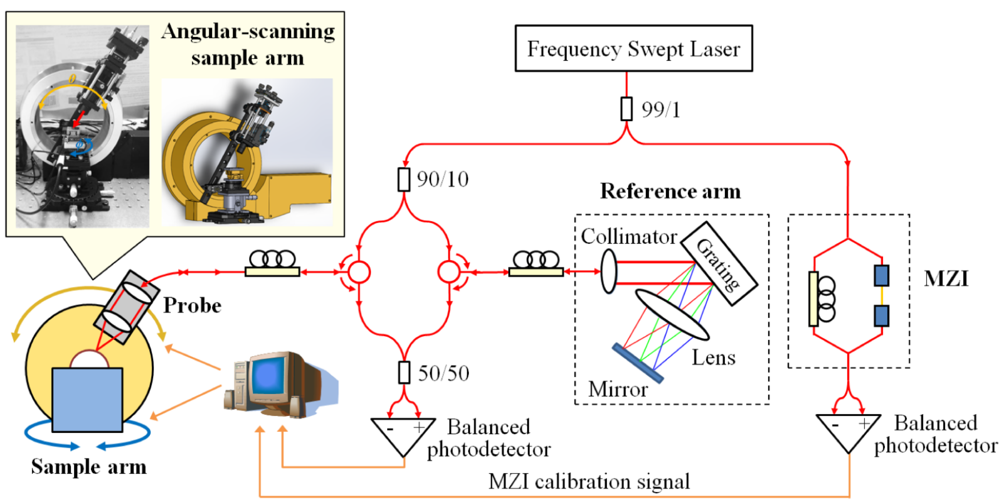

Fig. 2. Schematic layout of the angular-scan OCT system.

3.1 Characterization of the angular imaging space

The 3D imaging volume of the angular-scan OCT system is approximately a spherical dome spatially as illustrated in Fig. 3(b), neglecting any ray deviation upon incidence on a refractive sample. The outer boundary of the dome is characterized by a “zero optical delay sphere” that is formed by the azimuthal scans of the zero optical delay line on a cross-sectional image as shown in Fig. 3(a). The zero optical delay is defined by the same optical path length as the reference arm. The depth acquisition is approximately in the radial direction; the imaging depth was measured to be ~5 mm in air as defined by a −10 dB sensitivity roll-off of the system.

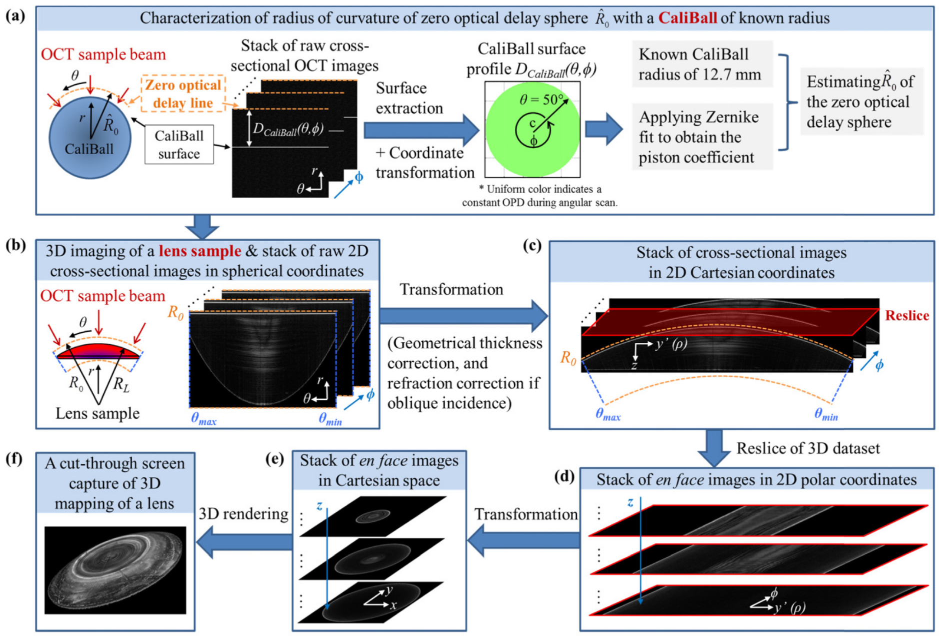

Fig. 3. Protocol of imaging space characterization (with a CaliBall), coordinate transformation, and 3D rendering of a lens sample acquired by the angular-scan OCT system (using normal incidence on the sample surface as an example).

It is essential to quantify the radius of curvature of the zero optical delay sphere in order for 1) quantitative assessment of the radius of curvature of a spherical sample under imaging and 2) further correct mapping of the 3D spherical-coordinate raw data set in Cartesian space for visualization. To characterize the radius of curvature of the zero optical delay sphere, a calibration sphere (i.e., CaliBall, Optical Perspectives Group, AZ, USA) was imaged with the sample beam scanning perpendicular to its surface. The CaliBall is a grade 5 spherical standard with a radius of 12.7 mm ± 20 nm and surface roughness < 5 nm. The angular scan covered ± 50° polar and 180° azimuthal scanning angles, respectively, as shown in Fig. 3(a). The resulting raw OCT images are a sequence of 2D cross-sectional frames acquired at a series of azimuthal angles. Each column on a gray-scale cross-sectional image corresponds to a depth *(r*) profile acquired at a polar (θ) scanning angle. The bright line on an image as shown in Fig. 3(a) represents the CaliBall surface. The optical path difference of the CaliBall surface relative to the zero optical delay line, measured along the sample beam path, can be extracted by an intensity peak detection algorithm. By applying the peak detection algorithm to the entire 3D imaging data set, the relative surface profile of the CaliBall, denoted as $D_{CaliBall}(\theta,\phi)$, is measured on an angularly evenly distributed (θ,ϕ) grid as shown by the green surface map in Fig. 3(a). It is evident that due to the concentricity of the CaliBall surface with the zero optical delay sphere, the $D_{CaliBall}(\theta,\phi)$ map is rather constant. By applying a lower order 36-term FRINGE Zernike polynomial fit (hereafter referred to as a Zernike fit) to $D_{CaliBall}(\theta,\phi)$ across the circular aperture, the piston coefficient may be

Optics EXPRESS

extracted to represent the radii difference between the zero optical delay sphere and the CaliBall. Combined with the known radius of the CaliBall, the radius of the zero optical delay sphere, denoted as $\hat{R}_0$, may be estimated.

Note that any residual longitudinal or lateral misalignment of the CaliBall from being exactly concentric with the zero optical delay sphere would be manifested as a power or tilt term in $D_{CaliBall}(\theta,\phi)$. In this case, the location of the Caliball relative to the zero optical delay sphere can be accurately computed by taking into account the coefficients of the power and tilt terms from Zernike fitting as well. The derivation of this algorithm is similar to that detailed in the Appendix of [4]. Therefore, the 3D imaging of CaliBall allows accurate estimation of the radius of curvature of the zero optical delay sphere, which will be in turn used for estimating the radius of curvature of the convex surface of an S-GRIN lens in a similar manner.

3.2 S-GRIN lens imaging setup and estimation of lens convex radius of curvature

With the radius of curvature of the zero optical delay sphere being calibrated with the CaliBall, the part on the sample platform was replaced by an S-GRIN lens for imaging. The convex lens surface was aligned to be concentric with the angular trajectory of the OCT θ-scanner probe. The reference mirror may remain at an unchanged optical path for the imaging of the new sample. However, it should be noted that the sensitivity of the system decays with increased distance from the zero optical delay path. In order to utilize the imaging depth range with optimal sensitivity, it is more advantageous to shift the zero optical delay sphere to a position immediately above the sample. To do so, the collimating lens in the reference arm of Fig. 2 was moved on a precision motorized linear stage (VP-25XL, Newport, CA, USA) along the optical axis. The accuracy of the stage was ± 1.0 µm. The amount of translation of the collimating lens, denoted as ΔD_R, was computed from the stage position readings. As a result, the optical path length (OPL) of the reference arm was changed by ΔD_R; the radius of curvature of the new zero optical delay sphere R_0 can be estimated as $R_0 = \hat{R}_0 - \Delta D_R$. R_0 was computed to be 20.23 ± 0.05 mm for this experiment. Note that the CaliBall calibration of the radius of curvature of the zero optical delay sphere as described in Section 3.1 is only required once for the angular-scan system (although a good metrology practice is to re-calibrate a system on a regular basis), provided that any change in the OPL of the reference arm is always recorded.

During the experiment of imaging the S-GRIN lens, the angular trajectory of the θ-scanner probe extends over ± 29° as shown schematically in Fig. 4(c) to cover the 19.3 mm full diameter of the lens. A cross-sectional raw image is shown in Fig. 4(a), where the top flat and bottom curved lines represent the convex and the plano surfaces of the lens, respectively. It can be seen that, under this imaging setup, only the layer structure near the center of the lens was captured where the sample beam is at exact or close to normal incidence. The rest of the internal structure is hardly visible due to the obliquity of the back-reflected beam that was far out of the collecting aperture of the objective lens, which also indicates that the internal layers of the S-GRIN lens are not concentric with its convex surface.

From the 3D imaging data set of the S-GRIN lens, the surface profile of the convex lens surface relative to the new zero optical delay sphere can be extracted by a peak detection algorithm and denoted as $D_{Convex}(\theta,\phi)$. By applying a Zernike fit to $D_{Convex}(\theta,\phi)$, the piston, power, and tilt coefficients, combined with the estimated radius of curvature of the zero optical delay sphere R_0, may be used to deduce the radius of the convex lens surface, denoted as R_L.

Alternatively to the first imaging setup of normal incidence on the convex surface, in order to image the entire layer structure, a slight oblique incidence of the sample beam on the

Optics EXPRESS

convex lens surface may be purposely introduced. In this way, the obliquity of the beam incidence on the internal layers that showed eccentricity from the convex lens surface was reduced, and thus the imaging SNR of the internal structure was enhanced. Figure 4(f) shows this modified imaging configuration. The S-GRIN lens was elevated by a vertical stage translating the sample platform such that the center of curvature of the convex lens surface was longitudinally shifted from that of the angular trajectory of the θ-scanner by about 6.9 mm. In this case, the θ-scanner swept ± 22° to cover the imaging of the full lens with the sample beam being at close to normal incidence on the internal layers as opposed to the surface. As a result, more internal structure within the lens was clearly revealed in the new raw image shown in Fig. 4(d).

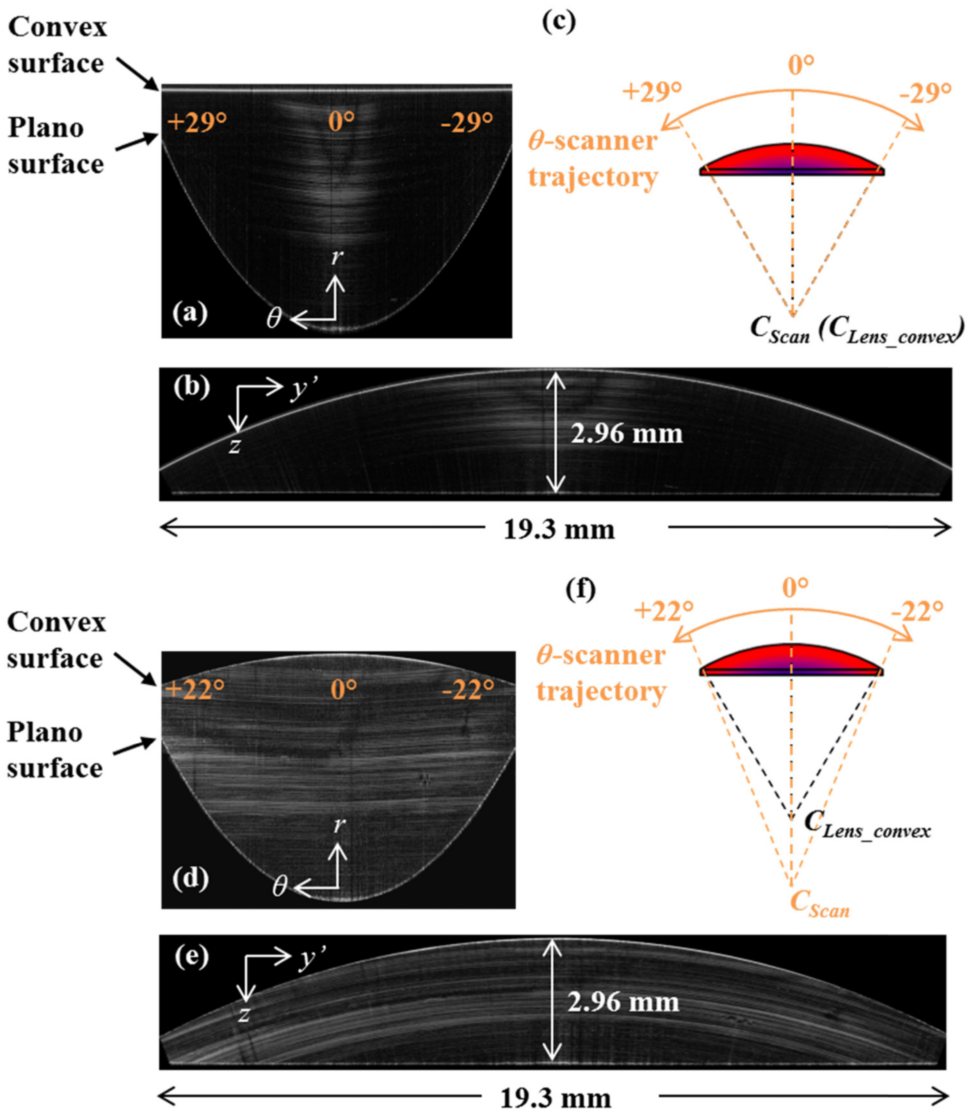

Fig. 4. (a) A raw 2D cross-sectional OCT image of a lens in polar coordinates and (b) remapped image in Cartesian coordinates, under the imaging condition shown in (c) where the θ-scanner trajectory and the convex lens surface were concentric. (d) A raw cross-sectional OCT image in polar coordinates and (e) remapped image in Cartesian coordinates, under the imaging condition shown in (f) where the θ-scanner trajectory and the convex lens surface were longitudinally shifted in their centers of curvature.

Optics EXPRESS

3.3 Refraction correction

To realize the 3D rendering of the S-GRIN lens imaged by the angular-scan OCT system, a mapping from spherical to 3D Cartesian coordinate system needs to be carried out, which we separate into two steps of 2D coordinate transformations on the cross-sectional slices and then the *en face* slices, respectively. The first step is the transformation of the raw cross-sectional images from polar to 2D Cartesian coordinates as shown in Figs. 3(b) and 3(c). Before presenting the transformation algorithm in the subsequent Section 3.4, we will first address the issue of refraction correction for the angular-scan OCT imaging in this section.

For the case of the sample beam scanning perpendicular to a sample surface, normal incidence eliminates the need to account for refraction at a media interface. However, any departure from normal incidence will require correcting the deviation of the optical path due to refraction at an interface of index change. Note that the r-θ cross-sectional images collected by the angular-scan imaging system contain the vertex of the nominally rotationally symmetric lens. In other words, the incident beam and the 3D lens surface normal are always considered coplanar, i.e., in the cross-sectional image plane. This allows for simplifying a 3D refraction correction model to a reduced, computationally-inexpensive 2D case without compromising physical rigor.

The most significant refraction of the beam occurs upon entering the convex lens surface from air, attributed to both the largest obliquity of the incident beam introduced on the surface and the largest refractive index difference at the air/lens interface as compared to the cases of beam incidence on internal GRIN layers. For the S-GRIN lens under inspection, the deviation angle of the beam upon surface refraction, which may be approximated as linear across the polar scanning field, reaches ~2.5° at ± 7.3° angle of incidence in the periphery of the aperture. In comparison, the typical angle of incidence of the beam on the internal layers is estimated to be within ± 1.5°; the deviation angle of the beam resulting from refraction at the interface of adjacent layers with 0.0015 phase refractive index change is ~0.1% of the incidence angle, i.e., < 5 arc-sec. This angular deviation of the beam falls well below the angular sampling resolution of the optical system (i.e., 0.2°) and therefore treated as negligible in our refraction correction model.

Figure 5(a) illustrates the refraction correction method that we developed for the angularly-collected spherical coordinate data. The orange dashed lines converging at the center of curvature of the scanning trajectory C_{Scan} represent uncorrected straight ray paths without accounting for refraction. By considering refraction at the convex lens surface, governed by Snell's Law, the corrected ray paths propagating in the lens are shown in blue solid lines. The corrected ray vectors are extended outside the lens in the drawing to converge at a new axial location C_{Ref}, which is actually the paraxial conjugate point of C_{Scan} (regarded as the "virtual object"). Note that this stigmatic imaging approximation is valid because of small angles of incidence on the convex lens surface and the S-GRIN layers across the lens aperture that were estimated in the last paragraph. It can be seen that, in our method, the refraction correction is equivalent to shifting the origin of the polar coordinate system by ΔC from C_{Scan} to C_{Ref}. Therefore, the refraction correction step may be conveniently combined in the polar to Cartesian coordinate transformation process, which will be further described in Section 3.4.

To reach a mathematical expression for the position of C_{Ref}, it is necessary to express the optical power P_L of the convex lens surface under paraxial approximation as

$$P_L = \frac{n-1}{R_L}, \tag{1}$$

where an average refractive index n is used here to represent the bulk lens material (assuming internal beam deviation is negligible), and R_L is the radius of curvature of the convex lens surface. The distance l_R of C_{Ref} from the lens convex vertex (i.e., the paraxial principal plane) can then be solved from the lensmaker's equation

$$P_L = \frac{n}{l_R} - \frac{1}{l_S}, \tag{2}$$

where l_S is the distance of C_{Scan} from the lens convex vertex. l_S may be computed from $l_S = R_L + \Delta l$, where Δl is the z-translation of the sample when departing from being concentric with the θ-scanner trajectory. Another alternative way to verify l_S will be shown in Section 3.4.

Substituting Eq. (1) into Eq. (2), we have

$$l_R = \frac{nR_L l_S}{l_S(n-1) + R_L}. \tag{3}$$

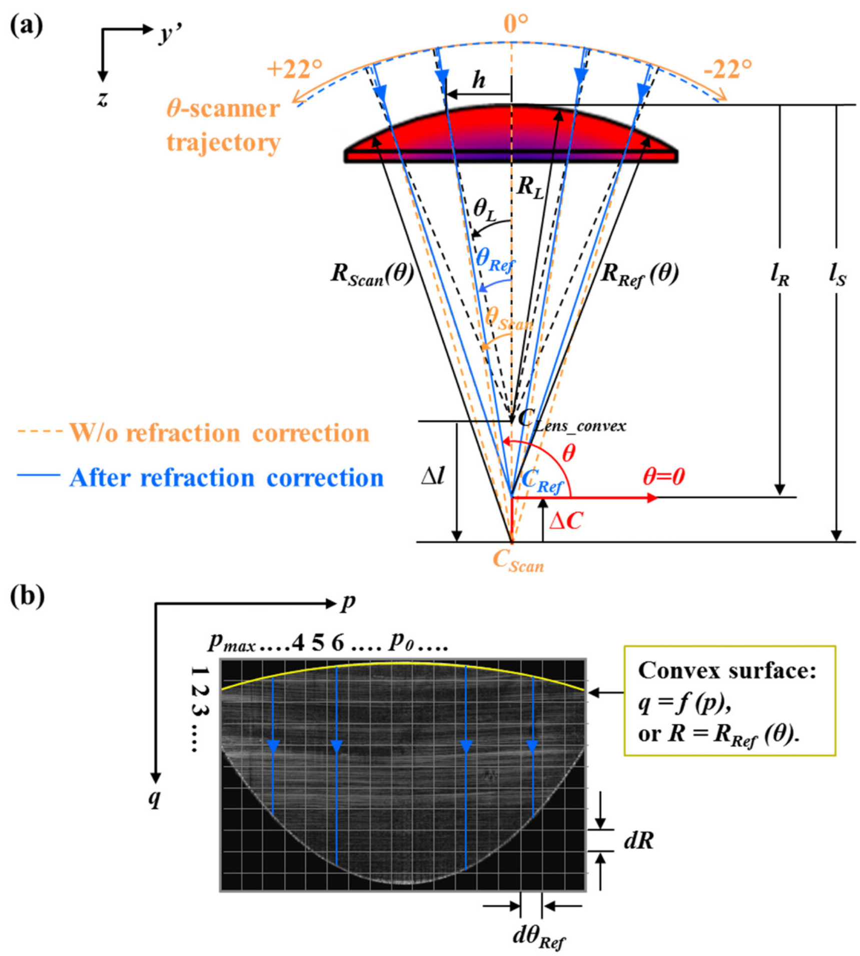

Fig. 5. (a) Illustration of the refraction correction strategy based on the angular-scan imaging setup. (b) Interpretation of a raw cross-sectional polar image obtained from angular-scan imaging.

Optics EXPRESS

3.4 Coordinate transformation of cross-sectional polar images

With the methodology of the refraction correction for the angular-scan OCT imaging worked out, we will demonstrate the associated polar-to-Cartesian coordinate transformation process that incorporates the refraction correction during assigning polar coordinates to angularly-collected frame data. As has been derived in Section 3.3, the polar coordinates prior to refraction correction are defined by scanning and thus with respect to the angular scanning origin C_{Scan}, whereas the new polar coordinates accounting for refraction correction are with respect to the new origin C_{Ref}. In this section, we will take the path of first deriving an expression for the radial coordinates of the contour of the convex surface with respect to the old and then the new polar origins. The mathematical expressions for the convex surface serve as a connection for remapping the radial coordinates of the entire frame. In terms of the angular correction, we will show that it can be simply achieved by introducing a refraction-corrected polar sampling resolution, considering the increased convergence of the ray fan after refraction. Note that the instance of the normal incidence on the convex surface is treated as a special case, for which l_S in the following equations may be replaced by R_L.

As shown in Fig. 5(b), denoting the row and column pixel dimensions as p and q, respectively, the contour of the convex (top) surface on a raw imaging frame may be segmented by intensity thresholding and mathematically expressed as $q = f(p)$ in pixel coordinates. Denote the scanning angle of the θ-scanner as θ_{Scan}, and the distance of the convex surface contour from C_{Scan} as $R_{Scan}(\theta_{Scan})$. If the index of the column corresponding to the normal incidence of the beam on the lens vertex (i.e., $\theta_{Scan} = 0$) is denoted as p_0, the relationship between p and θ_{Scan} can be expressed as

$$\theta_{Scan} = d\theta_{Scan} \cdot (p_0 - p), \tag{4}$$

where $d\theta_{Scan}$ is the polar sampling resolution defined in scanning. If the index of the column corresponding to capturing the very edge of the lens convex surface (i.e., $\theta_{Scan} = \theta_{Scan}^{\max}$) is denoted as $p_{\max}$, then

$$R_{Scan}(p = p_{\max}) = R_{Scan}(\theta_{Scan} = \theta_{Scan}^{\max}) = \frac{R_L \sin\theta_L^{\max}}{\sin\theta_{Scan}^{\max}}, \tag{5}$$

where $\theta_L^{\max}$ indicates the angle of the imaged lens edge referencing to C_{Lens_convex}. Thus, $R_{Scan}(p)$ for the entire yellow contour in Fig. 5(b) may be computed by analyzing the raw image as

$$R_{Scan}(p) = R_{Scan}(p_{\max}) + \left[f(p_{\max}) - f(p)\right] \cdot dR, \tag{6}$$

where dR is the radial sampling resolution used for imaging. It is apparent that $l_S = R_{Scan}(p_0)$.

Next, refraction correction will be considered. Denote the angle of the beam after refraction on the lens surface as θ_{Ref}. The stigmatic imaging ray transfer relation yields $n\theta_{Ref} = \theta_{Scan} - hP_L$, where the associated parameters are illustrated in Fig. 5(a). By plugging in P_L from Eq. (1) and noting that $h = -l_S \cdot \theta_{Scan}$, θ_{Ref} is solved from the ray transfer equation as

$$\theta_{Ref} = \theta_{Scan} \frac{(n-1)l_s + R_L}{nR_L}. \tag{7}$$

Taking the derivative of both sides, we have

$$d\theta_{Ref} = d\theta_{Scan} \cdot \frac{(n-1)l_s + R_L}{nR_L}. \tag{8}$$

$d\theta_{Ref}$ represents the refraction-corrected polar sampling resolution.

Based on geometrical relations, the distance of the convex surface from the refraction-corrected polar origin C_{Ref} , denoted as R_{Ref} , may be expressed as

$$R_{Ref}\left(\theta_{Ref}\right) = R_{Scan}\left(\theta_{Scan}\right) \cdot \frac{\sin\theta_{Scan}}{\sin\theta_{Ref}}. \tag{9}$$

Alternatively, by substituting Eqs. (4) and (7) into Eq. (9), it may be rewritten in terms of the pixel coordinate as

$$R_{Ref}\left(p\right) = \frac{R_{Scan}\left(p\right) \cdot \sin\left[d\theta_{Scan}(p_0 - p)\right]}{\sin\left[d\theta_{Scan}(p_0 - p)\dfrac{(n-1)l_s + R_L}{nR_L}\right]}. \tag{10}$$

Thus, each pixel indexed as $(p,q)_\phi$ within a 2D cross-sectional image taken at an azimuthal angle ϕ may be readily assigned with a pair of polar coordinates $(\theta,R)_\phi$ as

$$\theta(p,q) = (p_0 - p) \cdot d\theta_{Ref} + \frac{\pi}{2}, \tag{11}$$

$$R(p,q) = R_{Ref}(p) + \left[f(p) - q\right] \cdot dR. \tag{12}$$

Note that, in accordance with polar coordinate system conventions, the polar parameter θ_{Ref} is replaced by $\theta = \theta_{Ref} + \frac{\pi}{2}$ such that $\theta = 0$ corresponds to the horizontal axis as shown in Fig. 5(a). The origin of this polar coordinate system resides at C_{Ref} , which may be perceived as the refraction-corrected center of curvature of the angularly-scanned beam "wavefront".

It is apparent that the relations $y' = R\cos\theta$ and $z = R\sin\theta$ set the conversion from polar $(\theta,R)_\phi$ to Cartesian coordinates $(y',z)_\phi$. The notation of y' is adopted here to differentiate the horizontal axis of 2D Cartesian frames from the y axis in a 3D Cartesian coordinate system. Instead of the more straightforward forward mapping approach described by these two relations, we use inverse mapping to reconstruct the image in Cartesian space. Each target pixel in a Cartesian frame is allocated to a coordinate in the raw polar image; linear interpolations based on surrounding pixels in the raw image are thus applied to yield the target pixel value. Compared with forward mapping, inverse mapping provides the benefit of optimum computational efficiency by costing one transformation per target pixel.

3.5 Layer segmentation and geometrical thickness correction

It should be noted that the acquired OCT images are represented in terms of group optical path length, which is the product of the geometrical thickness and the group refractive index n_g [22]. Note that the group refractive index rather than the more commonly known phase refractive index is used here due to the low coherence interferometry nature of OCT. The group refractive index n_g is associated with the phase refractive index n_p by a dispersion relation $n_g(\lambda_i) = n_p(\lambda_i) - \lambda_i \left(\frac{\partial n_p(\lambda)}{\partial \lambda}\right)_{\lambda_i}$, where $\left(\frac{\partial n_p(\lambda)}{\partial \lambda}\right)_{\lambda_i}$ is the dispersion slope at an arbitrary wavelength λ_i.

To obtain the true-scale geometry of the sample, the imaged optical paths need to be scaled down by the corresponding group refractive index along the path. Thus, the 3D refractive index distribution within the imaging volume, i.e., $n_g(p,q)$, needs to be estimated. To compute $n_g(p,q)$, based on the stacking recipe of the film layers, ~29 layer sections with varying refractive indices were noted and segmented on the raw polar images. Note that each section is composed of 4 or 5 layers of the same composition. The refractive index of each section was estimated by assuming their conformity to the specifications. The group index profile of the lens estimated for each sample beam path was then used to scale the OCT-imaged optical thickness. In practice, this geometrical thickness correction step was performed simultaneously with the refraction correction, by substituting dR in Eq. (12) with pixel-dependent $dR'(p,q)$ computed as

$$dR'(p,q) = \frac{dR}{n_g(p,q)}. \tag{13}$$

To segment the 29 layer sections within the S-GRIN lens on the collected OCT images, a custom layer segmentation algorithm was developed to automatically detect the locations of these layer interfaces. Figure 6(a) overlays the contours of the segmented layer structure in green over a raw grey-scale cross-sectional polar image of an S-GRIN lens containing the lens vertex. The locations of the convex and plano surfaces of the lens were detected first by intensity peak detection within their respective location search ranges along each column. The locations of the inner layer section interfaces, which represent the boundaries where refractive index changes occur, were identified initially in the central column (i.e., $p = p_0$) by setting the search ranges for multiple peak detection based on the nominal layer locations in the lens center. The rest of the layer interfaces were then detected outward from the center to the periphery, based on intensity peak detection weighted by the detected layer interface location in the neighboring pixels. Note that a curve continuity constraint was enforced, such that the segmented contours were smooth, continuous, and accurately estimated. Since preferably non-overlapping search ranges were set for each of the layer interfaces, it is evident that features with strong curvature are disadvantageous for automatic, unambiguous segmentation of the layer interfaces. Thus, an additional benefit of the angular-scanning sample probe following the curvatures of internal layers is that the resulting images show naturally “flattened” layer interfaces, which ease the automatic segmentation of such structure.

Following the layer segmentation on the raw images, the identified layer interfaces were also mapped out on the reconstructed Cartesian space imaging data as shown in Fig. 6(b) for further evaluation of their geometrical properties. Note that the mapping of the layer interfaces on Cartesian frames was achieved by applying the same cross-sectional image transformation and correction algorithms as described in Sections 3.4 and 3.5 to the segmented layer interfaces on raw images.

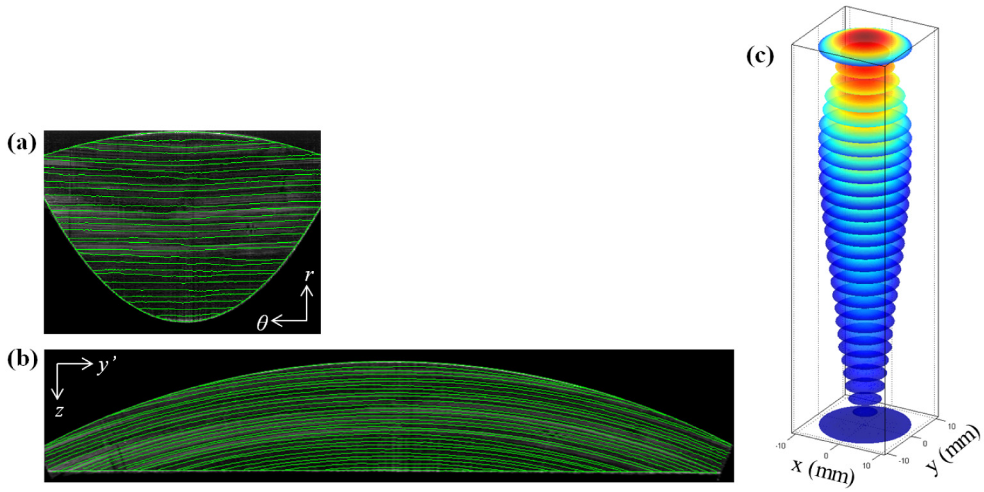

Fig. 6. (a) Layer section segmentation on a raw cross-sectional image of an S-GRIN lens. (b) Identified layer structure remapped in the reconstructed Cartesian S-GRIN image. (c) 3D topographies of segmented surfaces/ layer section interfaces (note that the topographies are purposely offset along z for better visualization).

3.6 Coordinate transformation of resliced en face images

Following the processing detailed in Sections 3.4 and 3.5, all cross-sectional y'-z slices indexed by the azimuthal angle ϕ are stacked to form a 3D data set, which is then re-sliced (ImageJ, National Institutes of Health, Bethesda, MD) along the z dimension to yield a sequence of *en face* $y'(\rho)$-ϕ slices indexed by z as shown in Fig. 3(d). The y' axes of the original cross-sectional images now become the radial spikes on each *en face* slice and therefore a new notation of ρ axis is adopted instead. A pair of polar coordinates $(\rho,\phi)_z$ may then be assigned to each pixel on an *en face* slice at z. By performing the second step of polar-to-2D-Cartesian coordinate transformation on each *en face* image using inverse mapping (Parallel Computing Toolbox, Matlab 2014b, MathWorks Inc., MA, USA), *en face* slices each represented in $(x,y)_z$ coordinates may be reconstructed, and readily stacked along z to form the final 3D data set in (x,y,z) coordinates as shown in Fig. 3(e). Further volumetric rendering of the data (Voxx software, Indiana University, IN, USA) enables true-scale 3D viewing of the sample with a representative screen shot shown in Fig. 3(f).

4. Results

During the experiment, the angular-scan OCT system was operated at the sampling resolutions of 0.2° for both polar (θ) and azimuthal (ϕ) dimensions and ~2 µm for the radial (r) dimension. Two different imaging conditions of normal and oblique incidence on the convex surface as described in Section 3.2 were carried out for collecting 3D data sets of the lens under test. Following the method described in Sections 3.4 – 3.5, polar-to-Cartesian transformations were performed. Two examples of the remapped Cartesian frames of the S-GRIN lens based on the two distinct imaging configurations are shown in Figs. 4(b) and 4(e), respectively. The imaging clearly shows the departure from concentricity between the convex lens surface and the S-GRIN distribution. Based on the method in Section 3.2, the convex radius was estimated to be 20.11 ± 0.18 mm. The convex radius was also measured by a precision spherometer to be 20.01 ± 0.25 mm, which validated the accuracy of the OCT measurement within ~0.5%. Additionally, the group optical path length of the part through its center thickness was measured over 100 repeated measurements to be 4.5365 ± 0.0005 mm.

Optics EXPRESS

Note that this level of accuracy in measuring the group optical thickness benefits from the ability of the FD-OCT system to simultaneously image both surfaces of the lens, and therefore is insusceptible to the vibration noise of the rotation stages. Assuming consistency of the average group refractive index with the theoretical value to an accuracy of ± 0.0001, the geometrical center thickness of the lens was then estimated to be 2.9617 ± 0.0004 mm.

A sequence of cross-sectional images acquired at different azimuthal angles was finally volumetrically rendered in true-scale 3D Cartesian space following the processing method detailed in Section 3. A video clip showing 3D viewing of the S-GRIN lens is presented in Visualization 1 with two screen captures shown in Figs. 7(a) and 7(b). Figures 7(c)-7(f) provide the *en face* images cut through the four planes of the lens as denoted by the red dashed lines in Fig. 7(a). Besides the spherical layer interfaces shown as the ring structure on the *en face* images, internal line and particle defects are clearly observed and sectioned at different depths. Their locations and sizes may be precisely identified in 3D. Further investigation of the nature of the defects may be explored with scanning electron microscopy for example, guided by OCT imaging. The partially dark region shown in Figs. 7(e) and 7(f) results from the substantial deformation of the local structure as opposed to being concentric spherical layers approximately perpendicular to the incident sample beam. The internal deformation of the part is likely caused by a non-symmetric flow of the GRIN layers during the preform molding process that, beginning with a square blank, may lead to the folding of planar layers around a sphere.

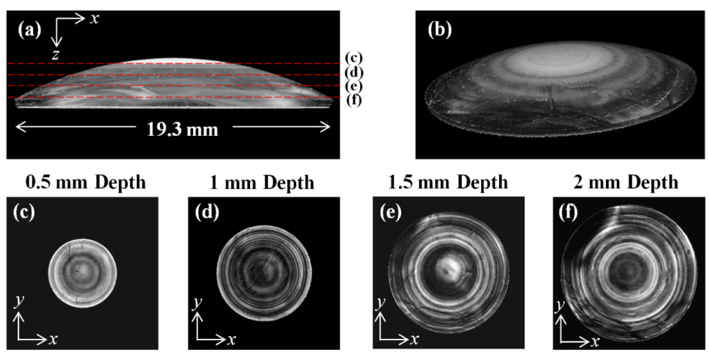

Fig. 7. (a) and (b) are snapshots of the 3D view of the S-GRIN lens based on a volumetrically rendered OCT imaging data set. (c-f) are *en face* images at 0.5, 1, 1.5 and 2 mm depth, respectively, as denoted by the red dashed lines in (a). A video clip of the volumetric rendering of the lens is presented in Visualization 1.

Meanwhile, to obtain quantitative evaluation of the internal structure of the S-GRIN lens, a layer segmentation algorithm was implemented on the raw cross-sectional frames to separate the 29 layer sections with varying refractive indices. The segmentation also yields an estimate of the 3D refractive index distribution $n_g(p,q)$ within the part when compared to the specified recipe. The segmented layer interfaces were mapped to their correspondence on the Cartesian images, after undergoing the same polar-to-Cartesian coordinate transformations that were applied to the cross-sectional frames accounting for both refraction correction and geometrical thickness correction, and then to the *en face* slices. The topographies of the reconstructed "true-scale" layer interfaces were finally obtained as shown in Fig. 6(c). Their best-fit radii of curvature and relative locations of the centers of curvature were further evaluated as shown in Fig. 8. The flatness of the bottom plano surface was evaluated to be ~2 waves RMS, which was within the manufacturing tolerance of the surface figure error. This result confirms the effectiveness of the refraction correction model. Figure 8(a) clearly shows significant longitudinal shifts in centers of curvature of the S-GRIN layers from that of the lens convex surface, which are on average ~3.9 mm. Yet, the internal S-GRIN layers are not concentric either; a gradual longitudinal shift in their centers of curvature accumulating to ~1.5 mm across the first 19 layer section interfaces (~2 mm geometrical thickness) being plotted is observed. Note that the radii of curvature of these S-GRIN layer interfaces also decrease by ~3.3 mm across a ~2 mm geometrical thickness, which falls more rapidly than being predicted by the specification as shown in Fig. 8(b). The aforementioned trends of the S-GRIN contours show quantitatively their departure from concentricity. This eccentricity defect was largely inherited from the thickness nonuniformity defect of a first-generation preform (the type of preform that the S-GRIN plano-convex lens so far reported in this paper was cut from) reported in [4]. This type of preform exhibited a bulk thickness increase from the center to the periphery and larger-than-specified radii of curvature due to mold alignment and figure errors in making the preform. The process of diamond turning the preform into the lens corrected for the error in the radius of curvature of the convex surface; however the process led to the significant longitudinal shift of the centers of curvature of the internal S-GRIN interfaces from that of the convex surface.

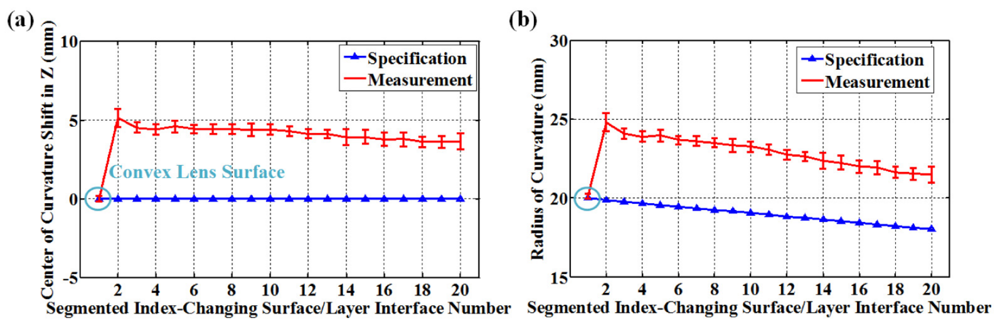

Fig. 8. The estimated (a) longitudinal shift in the centers of curvature and (b) radii of curvature of the first 20 segmented surface and layer section interfaces (i.e., with refractive index change on both sides).

To estimate the as-built performance of the manufactured S-GRIN lens caused by its dominant defect of departure from concentricity between the convex lens surface and the S-GRIN distribution, optical design software was used to model the lens, assuming a continuously varying S-GRIN profile. The as-built radius of curvature of the convex lens surface, the estimated average shift of the S-GRIN center of curvature from that of the convex surface (neglecting the eccentricity between the S-GRIN layers), and the actual center thickness, all measured by OCT as discussed previously, were fed into the S-GRIN optical model. A simulated interferogram representing a test plane wavefront transmitted through 98% aperture of the S-GRIN lens at 633 nm (double pass) was computed and shown in Fig. 9(a). As expected, the most notable aberration induced by the longitudinal shift of the centers of curvature of the S-GRIN inner interfaces from that of the surface geometry is spherical aberration. The Zernike primary spherical aberration was estimated to be 23.3 waves PV. The overall wavefront error was estimated to be 6.1 waves PV and 1.7 waves RMS. The lens was also experimentally tested on a He-Ne laser Fizeau interferometer (Verifire, Zygo Corporation, CT, USA) over 98% lens aperture based on an optical layout shown in Fig. 9(c). The measured transmitted wavefront interferogram is shown in Fig. 9(b), which agrees well with the simulation result in terms of a dominant Zernike primary spherical aberration of 19.4 waves PV. The overall wavefront error was measured to be 6.8 waves PV and 1.6 waves RMS. The "squarish distortion" of the interference fringes shown in the transmitted wavefront measurement can be linked to the "squarish" *en face* pattern qualitatively observed in the 3D angular-scan OCT imaging shown in Visualization 1. This indicates the internal deformation of the part likely attributable to a non-symmetric flow of the GRIN layers during the preform molding process, as discussed previously.

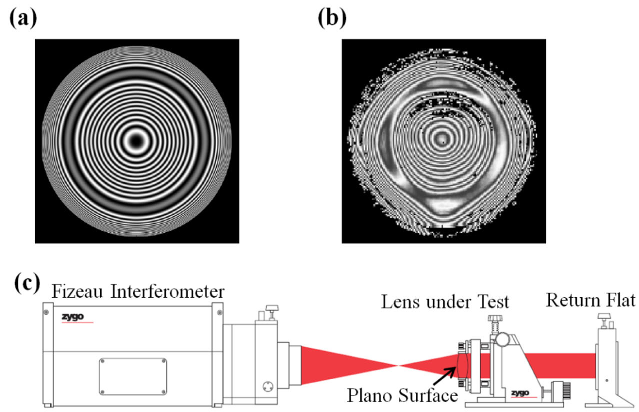

Fig. 9. (a) A simulated, approximate interferogram of the as-built S-GRIN lens. (b) An experimentally-obtained interferogram of the S-GRIN lens using the transmitted wavefront measurement configuration shown in (c). Due to the double-pass testing configuration, two fringes on an interferogram represent one wave of test part defect at 633 nm.

After the defects in the first generation of S-GRIN preform and lens were diagnosed by the angular-scan OCT and fed back to the manufacturer, new molds with improved quality were adopted for preform manufacturing; the manufacturing process was also fine-tuned guided by finite element analysis. Based on these OCT-enabled, targeted manufacturing process developments, newly manufactured S-GRIN lenses showed much improved optical quality. Figure 10 shows the interferograms of two new S-GRIN lenses measured with a Fizeau interferometer at 633 nm (double pass). It can be seen that the previous squarish artifact due to internal deformation is eliminated. The spherical aberrations of the lenses are much alleviated. The amount of Zernike primary spherical aberration for the two lenses is reduced to 4.5 and 2.9 waves PV, respectively, which for the latter corresponds to a 7x reduction in spherical aberration, and in both cases the improvement significantly increases the utilizable effective aperture of the lenses. The RMS transmitted wavefront errors are 1.3 and 0.8 waves, respectively, dominated by astigmatism. Note that some residual aberrations on the interferograms are trefoil due to mount-induced stress during alignment, which was validated by repeated measurements through rotations of the lens by 30 degrees.

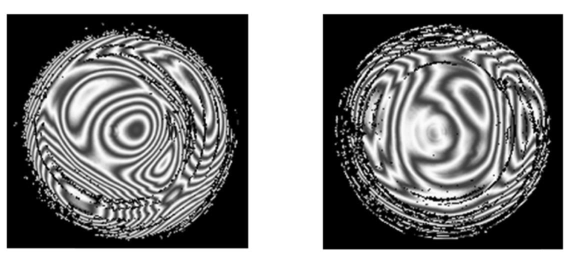

Fig. 10. Interferograms of two new S-GRIN lenses measured with a Fizeau interferometer.

5. Discussion

In Section 4, the accuracy of the surface and internal geometry of the old S-GRIN lens measured by the angular-scan OCT was indirectly validated by the transmitted wavefront test pointing to spherical aberration as a dominating error. The angular-scan OCT carries the advantage of probing into the internal structure of the lens that is immeasurable by classic interferometry. Note that conformity of the refractive index distribution of the lens to the prescribed specification was assumed in order to yield the calculations of the geometry of the lens from the OCT group optical path measurements. This assumption is based on our

Optics EXPRESS

previous work [21] where we investigated a confocal-scan OCT technique to simultaneously measure the refractive index and thickness profiles of flat, axial GRIN sheets. From the confocal-scan OCT experiments, we reached a conservative estimation that the refractive index profile of GRIN sheets conformed to the specification to an accuracy in the range of 10^{-4} – 5 x10^{-4}. This level of accuracy in the refractive index is expected to stand with the final S-GRIN lenses. An uncertainty on the order of 10^{-4} in the refractive index only results in negligible uncertainties in the lens geometry calculations, as compared to those caused by the group optical path measurement uncertainties. Therefore, it is valid to use the specification values as the estimated refractive index distribution of the lens.

For the old S-GRIN lens discussed in this paper, the longitudinal shift in the centers of curvature of the S-GRIN layers from that of the convex lens surface was detected by the angular-scan OCT to be on average 3.9 mm. While this may be considered as a mild eccentricity, the angular-scan OCT system is able to capture a much more significant shift in the centers of curvature of the curved S-GRIN layers and the lens surface. This is due to the high sensitivity of the OCT system in collecting not only back-reflected light but also back-scattered light. It should be noted though that the accuracy of the measurements depends on the SNR and the application of a refraction correction algorithm. For optimum SNR in probing the internal lens structure, the angular scanning trajectory of the θ-probe is best adjusted to provide near-normal incidence on the internal S-GRIN structure; the back-scattered signal from the outer lens surface will still be strong upon significantly oblique imaging angle, due to the large refractive index change from air to the lens material.

It should also be noted that, although the refractive index profile of the S-GRIN lens presented in this paper is radially linear, a broad range of lens samples with flexibly engineered layered refractive index distributions may be evaluated by the angular-scan OCT with the methodologies developed in this paper.

6. Conclusion

In this paper, we present a method for volumetric rendering and geometry metrology of an S-GRIN lens based on the high-SNR 3D imaging acquired by the angular scan OCT system we developed for advancing the manufacturing process of these S-GRIN optics. The 3D visualization enables nondestructive characterization of the internal structure of the lens for defect inspection, which guides manufacturing to achieve desired optical quality. The metrology demonstrates the capability for measuring the surface and internal geometry of a part including the radii of curvature of surfaces and internal layer interfaces, the part thickness, and the misalignment of the internal S-GRIN distribution with respect to the lens surface. The metrology results provided by OCT enable targeted manufacturing process development that brings about 7x spherical aberration reduction in the S-GRIN lenses from 19.4 waves PV to 2.9 waves PV. As a future perspective, the 3D mapping algorithm we developed, including the refraction correction, geometrical thickness correction, and coordinate transformations of angularly-collected data, may also be applied for the precision metrology of contact lenses [23], and to render general freeform samples with mild to potentially wild shapes where the angular-scan OCT system may be leveraged to provide high-SNR 3D imaging and metrology.

Acknowledgments

This work was supported by the Manufacturable Gradient Index Optics (M-GRIN) program of the Defense Advanced Research Projects Agency (DARPA) and the NYSTAR Foundation C050070. We thank Eric Baer for stimulating discussions and Stephen Head for his early contribution to mapping the angular scans into a 3D visualization. Finally, we thank the II-VI foundation for their support in OCT freeform metrology. This Research is synergistic with the NSF I/UCRC Center for Freeform Optics (IIP-1338877 and IIP-1338898).